Development of a new LiBr/LiOH-based alloy for thermal energy storage

Fouzia Achchaq, Elena Palomo del Barrio, Eric Lebraud, Stanislav Pechev, Jean Toutain

▶ **To cite this version:**

Fouzia Achchaq, Elena Palomo del Barrio, Eric Lebraud, Stanislav Pechev, Jean Toutain. Development of a new LiBr/LiOH-based alloy for thermal energy storage. Journal of Physics and Chemistry of Solids, 2019, 131, pp.173-179. 10.1016/j.jpcs.2019.04.001 . hal-02138899

HAL Id: hal-02138899
https://hal.science/hal-02138899

Submitted on 22 Oct 2021

HAL is a multi-disciplinary open access archive for the deposit and dissemination of scientific research documents, whether they are published or not. The documents may come from teaching and research institutions in France or abroad, or from public or private research centers.

L'archive ouverte pluridisciplinaire **HAL**, est destinée au dépôt et à la diffusion de documents scientifiques de niveau recherche, publiés ou non, émanant des établissements d'enseignement et de recherche français ou étrangers, des laboratoires publics ou privés.

Distributed under a Creative Commons Attribution - NonCommercial 4.0 International License

Version of Record: https://www.sciencedirect.com/science/article/pii/S0022369718323175
Manuscript_23eac14aeb3cb1bcc0eac58e8377b579

Development of a new LiBr/LiOH-based alloy for thermal energy storage

Fouzia Achchaq[1*], Elena Palomo del Barrio[2], Eric Lebraud[4], Stanislav Péchev[4], Jean Toutain[3].

[1]Bordeaux University, I2M UMR CNRS 5295, Esplanade des Arts et Métiers, 33 405 Talence, France
[2]CICenergiGUNE, Parque Tecnológico de Álava, Albert Einstein, 48, 01510 Vitoria-Gasteiz, Espagne
[3]INP Bordeaux, I2M UMR CNRS 5295, 16 Avenue Pey-Berland 33607 Pessac Cedex, France
[4]ICMCB, 87 Avenue du Docteur Schweitzer - 33608 Pessac Cedex, France

[*]*Corresponding email: fouzia.achchaq@u-bordeaux.fr*

Abstract

In this study, the LiBr/LiOH phase diagram and the key related thermodynamic properties of its specific compounds were theoretically and experimentally estimated (by thermodynamic modeling and differential scanning calorimetry experiments, respectively) and compared with previously reported results. The peritectic compound $Li_4Br(OH)_3$ was identified as a highly promising candidate for heat storage applications at around 300°C, mainly because of its outstanding energy density. As a precaution, the two limiting cases of thermodynamic solidification simulations (equilibrium and Scheil–Gulliver cooling conditions) were considered to confirm the relevance of synthesizing and experimentally studying this new potential heat storage material. After many tests and adjustments, a suitable synthesis protocol was developed and validated for characterizing the $Li_4Br(OH)_3$ compound using the X-ray powder diffraction technique. Preliminary thermal analysis was also performed for the successfully synthesized peritectic compound to confirm its high potential as a heat storage material. Our results indicate that it would be useful to comprehensive analyze the thermophysical properties of this material to assess its capacity for utilization in thermal energy storage applications.

Keywords: energy storage, LiBr/LiOH phase diagram, peritectic compound, thermodynamic property

1. Introduction

Considering current economic issues and energy problems, the development of new types of materials with potential applications in cost-effective compact thermal energy storage at high temperatures and over an extended range of temperatures is a technological challenge.

Gas–solid reversible reactions are particularly suitable for heat storage due to the simple separation of the gas released during heat absorption. Various types of gas–solid reaction systems have been investigated, including the dehydrogenation of metal hydrides (80–400°C), dehydration of metal hydroxides (250–800°C), decarboxylation of metal carbonates (100–950°C), and thermal desoxygenation of metal oxides (600–1000°C). The enthalpy of these reactions is usually extremely high, ranging from 400 up to 1100 kWh/m^3 depending on the temperature, but the feasible energy density is only between 200 and 500 kWh/m^3. This is because several problems remain unsolved such as a tendency for the solid to agglomerate, poor heat transport characteristics, low reaction kinetics, possible crystallization after dehydration, and sintering at high temperatures [1]. Thus, thermochemical heat storage development is still in a fundamental, laboratory stage and no proven designs and materials have yet progressed to a commercial scale.

At present, the commercially available high temperature thermal energy storage systems are exclusively sensible heat storage systems for use with single phase heat transfer fluids, including pressurized water, oils, molten salts, or gaseous fluids such as air or flue gas. Heat storage in molten salts is the main technique employed in the current solar power applications. The most widely used salt systems are two ternary systems: (i) Hitec comprising 40% $NaNO_2$-7% $NaNO_3$-53% KNO_3 and (ii) HitecXL comprising 48% $Ca(NO_3)2$-45% KNO_3-7% $NaNO_3$, both of which are used in a temperature range of 142–450°C; and (iii) the binary system called Solar Salt comprising 40% KNO_3-

© 2019 published by Elsevier. This manuscript is made available under the CC BY NC user license
https://creativecommons.org/licenses/by-nc/4.0/

60% $NaNO_3$, which is used in a temperature range of 240–600°C. Their achievable energy densities range from 30 to 70 kWh/m^3 [2].
The technology is still under development for use in latent heat storage systems with high temperature applications. In particular, many studies have investigated the selection and/or characterization of phase change materials for high temperature latent heat storage systems, particularly to allow the rapid integration and simple use of renewable energies [1-3]. This interest is explained by the capacity of phase change materials to store sensible heat but also because they can store latent heat isothermally to allow the development of compact and cost-effective thermal energy storage systems. Indeed, latent heat storage allows large amounts of energy to be stored in relatively small volumes compared with sensible heat storage systems, where the achievable volumetric energy density ranges from 80 kWh/m^3 to almost 200 kWh/m^3. In the temperature range from 120 to 320°C, saturated steam storage systems based on nitrates have been developed as phase change materials as well as the so-called "sandwich concept" for heat enhancement [3], and these methods are in the pre-commercial stage. However, the specific capacity is moderate (80 kWh/m^3) and the investment cost depending on the steam pressure is still high at 100–250 €/kWh.
The interest in the development of new thermal energy storage materials has led to a wide range of potential candidates. Indeed, more than 100 potential candidates have been identified for heat storage applications in the temperature range limited to 120–400°C [4]. In addition, several methods are available for selecting thermal energy storage materials for engineering and research in order to measure and/or analyze the thermal storage characteristics of materials, including experimental methods, theoretical calculations, and numerical simulations [2-8]. However, despite major progress in making experimental studies (e.g., high temperature generation, measurement and control devices, and corrosion-resistant and heat-resistant containments) and thermodynamic calculations self-compatible and complementary, the data stored with digital tools must be more reliable, sufficiently accurate, and updated periodically to ensure that appropriate materials are selected. Indeed, in terms of phase diagram construction, the calculations are usually validated based on insufficient experimental results because of discrepancies and missing details in published studies, even for “simple” binary compound stoichiometry. Moreover, the available phase diagrams were mainly prepared for equilibrium conditions, which are generally unrealistic. Therefore, it is necessary to "make the database developers aware of the importance of basic thermophysical property measurements and to make the related database more complete for the new materials development process" [2].

To the best of our knowledge, the LiBr/LiOH binary system has never been considered in reviews of salt-based phase change materials for thermal storage applications at medium and high temperatures (120–1000°C) [2-5]. In this study, we theoretically and experimentally estimated the LiBr/LiOH phase diagram, and compared the results with previously reported studies. First, the LiBr/LiOH phase diagram and the key thermodynamic properties of its specific compounds were theoretically studied using FactSage 7.0® thermodynamic software (CALPHAD-based method). The main thermophysical properties such as the transition temperature, phase change enthalpy, and density of the identified compounds (eutectic, peritectic, and peritectoid) in the optimized LiBr/LiOH phase diagram were assessed in order to confirm their capacity to meet the requirements for use in applications including direct steam generation solar thermal plants (~300°C). The LiBr/LiOH phase diagram was then experimentally established using differential scanning calorimetry (DSC). Comparisons of the performance of the identified compounds allowed the selection of the stoichiometric peritectic compound with potentially the highest thermal energy density. Indeed, we showed that its predicted characteristics were better than that of the LiOH/KOH binary system, which has the highest enthalpy of change (535 J/g) for a transition temperature of 315°C according to a previous study [4]. As a precaution, the two limiting cases of thermodynamic solidification simulations (equilibrium and Scheil–Gulliver cooling conditions [9]) were considered to check the relevance of synthesizing and experimentally studying this new potential heat storage material. After confirming that the

stoichiometric peritectic compound is of potential interest for specific applications, the experimental synthesis protocols were investigated. After many tests and adjustments, a suitable synthesis protocol was developed and validated using X-ray powder diffraction. Preliminary thermal analysis was also performed for the successfully synthesized compound in order to assess its high potential as a heat storage material.
All of these steps confirmed that this new LiBr/LiOH-based alloy is a highly attractive and competitive thermal energy storage material, which merits further investigation in future research.

2. Methodology

2.1. Thermodynamic modeling of the LiBr/LiOH system

The development of a new LiBr/LiOH-based alloy was performed using FactSage 7.0® software, which is based on the CALPHAD method [10], in order to facilitate a rapid design process by considering specific compositions and heat treatments. This method allows the phase diagram of interest to be established for equilibrium conditions by calculating the related thermodynamic functions and parameters using Gibbs energy minimization. The Gibbs free energies for all phases of the system were calculated as functions of the temperature, composition, and pressure using previously reported experimental data and suitable Gibbs free energy mathematical models [11]. The LiBr/LiOH stable phase diagram was calculated using model parameters collected from the thermodynamic molten salt database. The specific compounds were identified (eutectic, peritectic, and peritectoid) and the main thermophysical properties (e.g., transition temperature, phase change enthalpy, and density) had to satisfy the requirements for use in a suitable thermal storage system. Comparisons of their performance allowed us to select the stoichiometric peritectic compound with the potentially highest thermal energy density. As a precaution, the two limiting cases of thermodynamic solidification simulations comprising equilibrium and Scheil–Gulliver cooling conditions were considered to confirm the relevance of synthesizing and experimentally studying this new potential heat storage material. Hence, the enthalpy-temperature function was calculated for these two limiting cases of the solidification process.

2.2. Experimental LiBr/LiOH phase diagram determination

2.2.1 Salt-dependent synthesis protocols

Anhydrous powders of LiBr and LiOH supplied by Acros Organics were used to prepare binary mixtures. The properties of the chemicals supplied by Acros Organics and those calculated using FactSage 7.0® software are shown in Table 1. The differences in the melting points of the salts were related to their purity and this was considered during the modeling process [12].

Chemicals	LiBr		LiOH	
Supplier	Acros Organics	FactSage 7.0®	Acros Organics	FactSage 7.0®
Purity (%)	99+	-	98	-
Molar mass (g/mol)	86.84	86.845	23.95	23.948
Fusion temperature (°C)	552	549.85	462	477

Table 1 Comparison of the molar masses and fusion temperatures provided by the supplier of the chemicals and the values obtained from the FactSage software database for each chemical.

Eleven compositions were selected for experimentally screening the whole composition range. Specific points that appeared in the theoretical phase diagram were considered, such as the eutectic,

peritectic, and peritectoid points, and tested using a DSC device (TG-DSC Sensys 3D, Setaram) (Table 2).

Composition	LiBr/LiOH (mol%)	LiBr/LiOH (wt%)	ΔH (J/g)	T_{Tr} (°C)	T_L (°C)
1. LiBr	100/0	100	203	-	549.85
2. Eutectic	58/42	83/17	-	244.12	266.69
			436	266.69	
3. Li_2BrOH	50/50	78/22	2.00	244.12	284.02
			366	266.69	
4.	37/63	68/32	-	244.12	303.90
			212	266.69	
5.	29/61	60/40	35.0	244.12	355.78
			244	266.69	
			495	303.90	
6. $Li_4Br(OH)_3$	25/75	55/45	803	303.90	379.89
7.	16/84	50/50	733	303.90	397.60
8.	29/61	40/60	587	303.90	426.00
9.	6/94	20/80	293	303.90	459.72
10.	1.4/98.6	5/95	70.0	303.90	473.66
11. LiOH	0/100	100	875	-	477.00

Table 2 Thermophysical properties of the compositions used to experimentally screen the whole composition range of the LiBr/LiOH binary system based on the calculated phase diagram. T_{Tr} is the transition temperature for each defined composition. T_L is the corresponding liquidus temperature (cf. Fig. 3).

The first step involved determining appropriate operating conditions in terms of the crucibles employed and the mass of the sample. Samples containing different ratios of each compound were weighed using a Mettler XP6U ultra-microbalance (precision = 0.02 mg), ground in a mortar, and placed in standard DSC crucibles, i.e., aluminum and Al_2O_3 crucibles. Each crucible containing a sample was placed into the DSC device. Unfortunately, preliminary tests failed because both types of crucibles were damaged by strong corrosion due to the salts and a creeping phenomenon. A closed stainless steel crucible was finally used. All of the crucibles were cleaned with acetone, deionized water, soaked briefly, and then dried before use. The crucibles exhibited no observable corrosion throughout the experiments. A glove-box containing an argon controlled atmosphere was used to avoid oxidation or hydration of the mixtures. After many tests, the final compound could not be extracted correctly from the crucible because the sample weight was excessively small. The minimum amount of each composition that was finally placed in the closed stainless steel crucible was the smallest amount (50 mg) that could be extracted correctly from the crucible for further characterization. The next step involved identifying a successful synthesis protocol. Different DSC protocols were established to synthesize the peritectic compound with the highest purity possible and with a sufficient amount when no leakage occurred. The best results obtained for the eutectic and peritectic transitions using this protocol are shown in Fig. 1, which illustrates the theoretical gravimetric energy density (difference between enthalpy and enthalpy of reference) as a function of the LiOH mass fraction according to experimental and theoretical estimations. The two curves exhibited the same trend but the experimental values were lower than the predicted values by about 75% because of leakage during the experiments, as shown previously for salt-based eutectics [13].

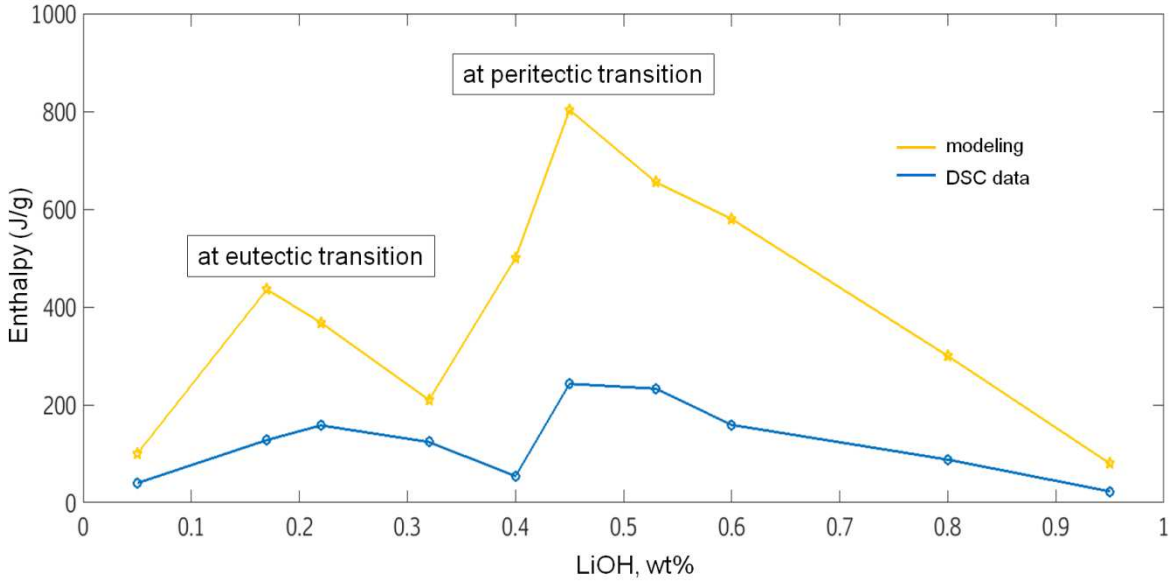

Figure 1. Gravimetric energy density dependence according to the LiOH mass fraction considering only the peritectic and eutectic transitions (the calculated values are the difference between the enthalpy and enthalpy for the reference in yellow and the DSC data in blue).

A new synthesis protocol was then tested using a free-cooled furnace (N120/85HA, Nabertherm) with no time constraint regarding the cooling process. Several temperature protocols were tested until the successful synthesis of a fairly pure peritectic compound (> 98%). The protocol can still be optimized further but it involves increasing the temperature from ambient up to 50°C above the liquidus temperature of for composition at a scanning rate of 2°C/min. The maximum temperature was then maintained for a holding time of 12 h before decreasing to the ambient temperature. The sample was kept inside the free-cooled furnace until it cooled completely, thereby allowing it is reach thermal equilibrium.

Powder X-ray diffraction (XRD) analysis was conducted to confirm the presence of the stoichiometric peritectic compound of interest. The crystal structure was determined based on XRD data collected at room temperature with a PANALYTICAL X'PERT 3 Powder diffractometer using MoK α radiation (λ = 0.71073 Å). Due to the hygroscopicity of the salt samples, they were ground and mounted in capillaries inside the argon-filled glove box to prevent atmospheric contamination.

2.2.2. Thermal analysis of the stoichiometric peritectic compound

The LiBr/LiOH phase diagram was determined by placing each sample into the DSC device to determine its transition temperature and enthalpy of change. First, the DSC was calibrated using the stainless steel crucibles and indium, tin, lead, zinc, and aluminum as standard materials with purities of 99.99% or greater. The device was then calibrated at a heating and cooling rate of 5°C/min over a temperature range corresponding to the predicted liquidus temperature ranges for the various LiBr/LiOH compositions. Each sample was then placed inside the DSC furnace with a dry argon flow at 30mL/min to ensure that the crucible remained in an inert atmosphere. The maximum value of the applied program temperature corresponded to the highest melting temperature for the 11 compositions investigated (475°C). The temperature program cycle was as follows: (i) from ambient temperature to 475°C at a scanning rate of 5°C/min in the DSC furnace; (ii) maintaining the maximum temperature for 45 min; and (iii) decreasing to ambient temperature at the same scanning rate of 5°C/min. Different scanning rates were tested with various compositions, i.e., 0.5, 2, 5, 10, and 50°C/min with holding times of 10, 30, 45, and 60 min. No significant differences were observed in the signals obtained at 0.5, 2, and 5°C/min with holding times of 45 and 60 min. Thus, a scanning rate of 5°C/min and holding time of 45 min were selected for optimizing the experimental time. The DSC measurements (heat flow versus temperature) were repeated at least three times for each sample. Only phase signals that appeared in all temperature cycles for all samples were considered and reported.

The enthalpy-temperature function was very time consuming to establish, so our efforts then focused on the most promising component. Two series of experiments with samples weighing 15.32 ± 0.02 mg and 15.45 ± 0.02 mg were conducted in the DSC device under a dry argon flow at 30 mL/min but in the isothermal stepscan mode. After a first cycle related to the synthesis of the compound for the first two samples (as described above), successive and repetitive sequences of short heat–hold segments were applied from 240°C to 450°C. These experiments did not succeed but they allowed us to improve the protocol, as explained in Subsection 3.3. Hence, a third sample weighing 95.00 ± 0.02 mg was prepared using the furnace by following the protocol (Subsection 2.2.1). The temperature increase was 1°C at a scanning rate of 0.5°C/min. The holding time was 60 min and the temperature varied from 260°C to 360°C around the peritectic temperature to ensure that the sample reached thermal equilibrium. The heat capacity obtained then reflected the reversible transformation of the sample. Finally, the temperature was decreased from 360°C to 200°C at a scanning rate of 0.5°C/min, and then from 200°C to ambient temperature at a scanning rate of 10°C/min.

3. Results and discussion

3.1. Calculated vs. experimental LiBr/LiOH phase diagrams

Figure 2 shows the theoretical changes in the gravimetric heat density (Fig. 2a) and the volumetric heat density (Fig. 2b) as functions of the LiOH mole fraction, and for temperatures between 200°C and 600°C. The changes in the heat density related to the transitions occurring at the eutectic and peritectic temperatures are clearly visible in Fig. 2. The peritectic compound had a higher heat density than the eutectic compound. In addition, the conversion of the gravimetric heat density into the volumetric heat density also confirmed its capacity to deliver the minimum storage volume. The calculations considered the density ρ of the system as $\rho = \rho_{min}$ (ρ_s was slightly below the peritectic temperature at the stoichiometric composition and ρ_L was slightly above the peritectic temperature at the stoichiometric composition; Fig. 3) in order to avoid overestimation.

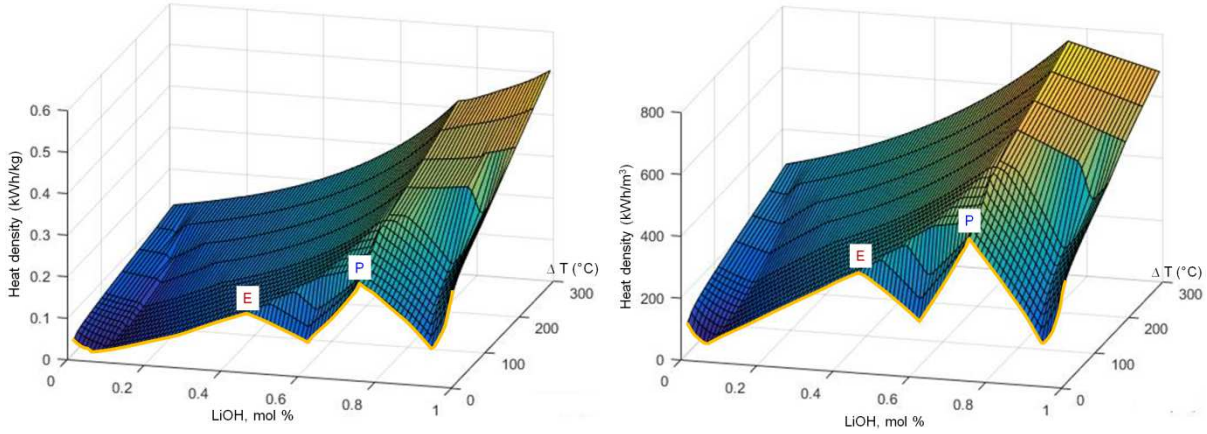

(a) (b)

Figure 2. Dependence of the theoretical heat densities on the LiOH molar fraction at ambient pressure and for a temperature variation of ΔT = 300°C: a. gravimetric heat density; b. volumetric heat density.

The values of the key thermophysical properties required for heat storage materials are shown in Table 3 for the specific compounds identified in the calculated LiOH/LiBr phase diagram to compare their performance. Given the need to trade-off the highest energy density and the lowest possible volume expansion, $Li_4Br(OH)_3$ was clearly more promising compared with the other compounds.

Compound	LiBr/LiOH (mol%)	LiBr/LiOH (wt%)	ρ_L (g/cm^3)	ρ_S (g/cm^3)	ΔV/V (%)	T_m (°C)	ΔH (J/g)	E (kWh/m^3)

LiBr	100/0	100	2.871	3.464	-	549.85	203	195
Eutectic	58/42	83/17	-	2.373	15	266.69	436	287
Li_2BrOH	50/50	78/22	-	2.671	-	244.12	2.00	1.51
$Li_4Br(OH)_3$	25/75	55/45	-	1.945	9	303.90	803	434
LiOH	0/100	100	1.582	3.464	-	477.00	875	356

Table 3 Key thermophysical properties of specific compounds observed in the calculated phase diagram.

The data obtained experimentally by Hartwig et al. [13] and Scarpa [13] were used to calculate the optimized LiBr/LiOH binary system phase diagram with the least-squares optimization method [11-15]. The diagram satisfied all of the requirements of the thermodynamic constraints related to the equilibrium conditions, as shown in Fig. 3. The data obtained from the DSC experiments are presented in the same graph and they are in relatively good agreement, except for the values above the calculated liquidus on the LiBr side. The other transition lines were not reported by Hartwig et al. [13] and Scarpa [13] but they could be estimated, although they should be determined with another method.

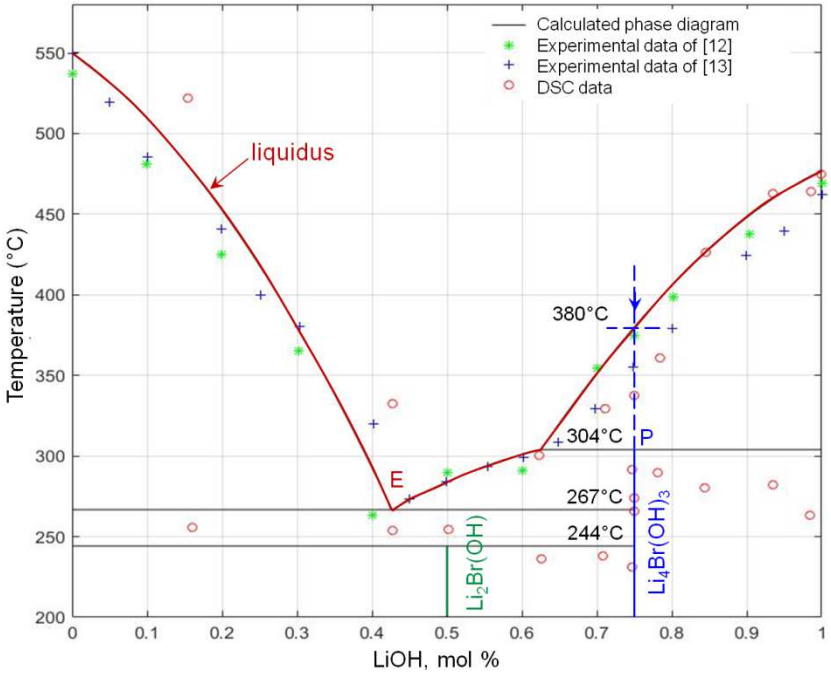

Figure 3. DSC data (red circles) and previously reported values (blue and green points) overlaid in the LiBr/LiOH binary system phase diagram calculated for equilibrium conditions at ambient pressure (liquidus line in red). The desired nominal alloy composition is highlighted by the blue dashed line.

As described in Subsection 2.2.1, a leakage phenomenon was observed during the DSC experiments at the level of the thread pitch in the crucibles. However, although a significant mass loss often occurred, which affected the signal strength and changed the composition of the sample, two other major reasons also required changes to the experimental strategy. First, insufficient details were available to obtain a reliable optimized LiBr/LiOH phase diagram. Experimental data for the liquidus were obtained by thermal analysis but there is disagreement [11] about the determination of the eutectic transition temperature, where previous studies reported temperature of 275°C [14], 243–245°C [15], and 250–278°C [16]. Thus, an uncertainty of ± 20°C could be assigned to the calculated diagram, which is very high [10]. The disagreement regarding the number and identity of the intermediate compounds was more obvious. According to Liu et al. [13], $Li_2Br(OH)$ melts peritectically at 245°C whereas Kroupa [11] stated that $Li_2Br(OH)$ is actually a peritectoid with a subsolidus transition temperature of 244°C. Furthermore, the compound $Li_5Br_3(OH)_2$ was unknown until 2003, and thus it was not considered by Kroupa [11], but it has now been structurally characterized [17]. The $Li_3Br(OH)_2$ phase was

structurally characterized in 1970 [13] but it has not yet been considered in the phase diagram modeling process [18].

The second reason is related to the solidification conditions used to establish the calculated phase diagram. As mentioned previously, the equilibrium conditions were considered but they could not be applied during our experiments, as explained in Subsections 2.2.1 and 3.2. Indeed, the equilibrium conditions involved allowing sufficient time for the material to gradually develop its final properties by considering the thermal equilibrium between the liquidus and solidus temperatures. The gradual changes in the phase compositions during cooling were then easily determined using the standard level rule (Fig. 4a). However, the experimental path in the quasi-equilibrium series was barely achieved by the material because of the time required, although determining a material's properties at equilibrium is of interest because it represents an upper limiting case for reference [8].

The non-equilibrium conditions are generally represented by the original Scheil–Gulliver model [19], which describes the solute (LiOH + LiBr) redistribution during the solidification process (1):

$$(1-k)C_L^{eq}df = (1-f)dC_L^{eq}, \quad (1)$$

where $k \equiv C_S/C_L$ is the segregation coefficient, if any, df is the fraction of the solidified solid phase, and C_L^{eq} is the liquid composition at equilibrium. It is assumed that no diffusion occurs in the formed solid phase whereas the remaining solute redistribution in the liquid occurs infinitely rapidly because both interstitial and substitutional species are involved [20]. It is also assumed that a thermodynamic equilibrium is maintained at the moving solid/liquid interface during solidification [21]. The potential back-diffusion phenomenon is also not considered, i.e., rapidly diffusing elements in the solid phase. The Scheil–Gulliver conditions are the worst case for microsegregation and they represent the lower limiting case for reference. Hence, these conditions are more realistic from an experimental viewpoint. Indeed, some issues can prevent the material from full formation such as solid-state diffusion slower than the solidification rate, or a wide range for the solid solubility of the crystallizing phases. For both approximation methods, the nucleation and growth phenomena as well as the related kinetic data are missing, and thus other advanced solidification models can be used. However, the Scheil approximation remains the best alternative for assessing a realistic reaction path [8] because it matches well with the industrial cooling conditions. The main impact of the stoichiometric peritectic compound on the synthesis process was a major difference between the targeted composition and that finally obtained. At equilibrium, the final compound was homogeneous but it had the expected final composition (Fig. 4a). From an energy viewpoint, the energy density related to the peritectic reaction could be exploited for thermal energy storage. By contrast, in the case of Scheil–Gulliver cooling, the material obtained was both temperature step-dependent and inhomogeneous because it formed layered solid phases with different compositions from the pro-peritectic to the eutectic phases (Fig. 4b). The heat energy storage potential may be strongly affected as a consequence.

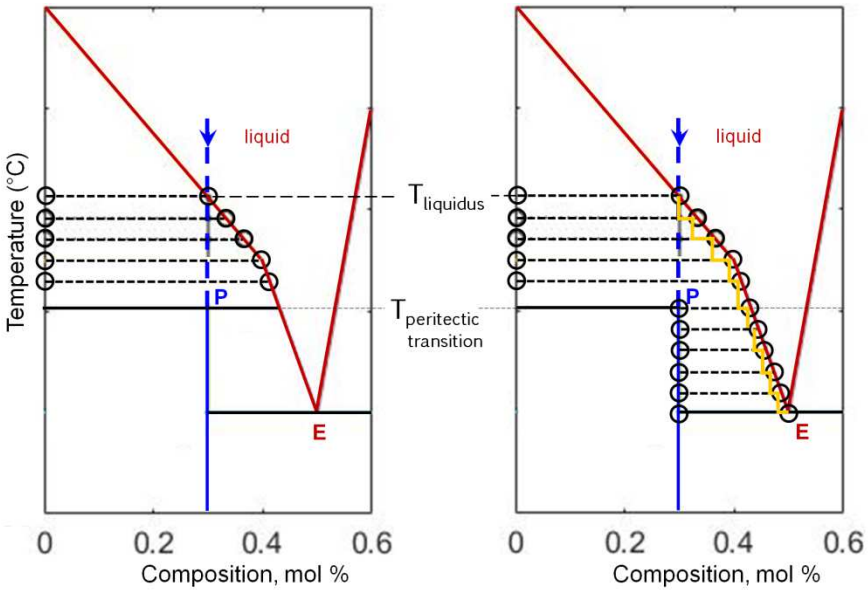

(a) (b)

Figure 4. Paths in the series of: (a) quasi-equilibrium steps (level rule) from the liquidus line to the peritectic transition, and (b) of out-of-equilibrium steps (Scheil–Gulliver) from the liquidus line to the eutectic transition.

3.2. Validation of the synthesis protocol for the stoichiometric peritectic compound

The new experimental strategy for obtaining $Li_4Br(OH)_3$ with potentially the highest energy density is described in Subsection 2.2.1. The XRD results obtained for the material are shown in Fig. 5. A recent study experimentally demonstrated that a $Li_4Br(OH)_3$ phase exists and a matching crystal structure was proposed to support the stoichiometry of this compound [22]. The XRD diagram indicated a strong match between the synthesized compound and its coexistence with trace LiBr-H_2O (< 2%), and the symmetry of the indexed pattern had a very strong match with P 1 21/m 1 type systems. Further research is required to synthesize a larger amount (~ 10 g) of $Li_4Br(OH)_3$ and to characterize its thermodynamic and thermophysical properties.

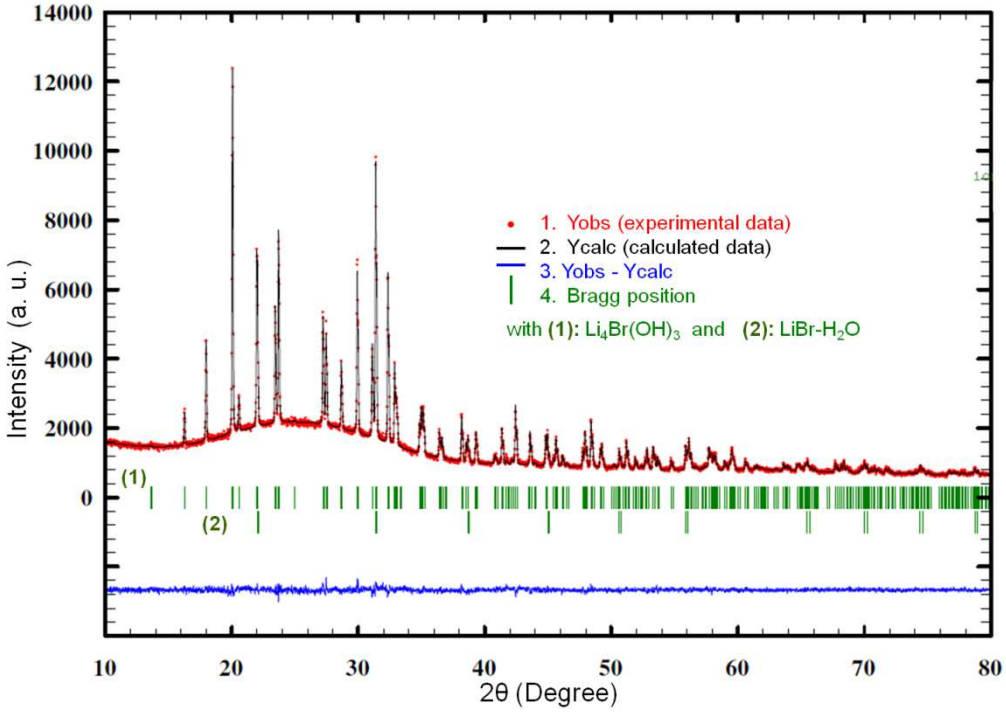

Figure 5. Rietveld plot of $Li_4Br(OH)_3$ showing the measured intensity (red points) and calculated intensity (black line) at the top, and the Bragg positions and plot of differences at the bottom.

3.3. Calculated vs. experimental changes in the enthalpy of $Li_4Br(OH)_3$ with temperature

Figure 6 shows the theoretical evolution of the phase fractions as functions of temperature for the fixed $Li_4Br(OH)_3$ composition under thermodynamic equilibrium and Scheil–Gulliver cooling conditions. The calculated curves showed that for 1 g of the liquid mixture at a starting temperature of 450°C, the phase fractions developed in the same manner under both applied conditions up to the liquidus temperature of 380°C. Subsequently, the amount of the liquid mixture decreased with the growth of the primary crystallizing LiOH phase fraction, which reached 20% of the total at the peritectic temperature (304°C) in both cases. At the end of the equilibrium cooling range, the LiOH solid fraction reacted isothermally with the remaining liquid at 304°C to form 100%wt $Li_4Br(OH)_3$. The Scheil–Gulliver cooling range (113°C) was wider than the equilibrium range (76°C). The peritectic reaction and transformation occurred at 304°C and ended isothermally at the eutectic temperature (267°C) (Subsection 3.1). Finally, the remaining liquid was completely consumed and the predicted amount of $Li_4Br(OH)_3$ was only 55%wt, with 20%wt of the remaining pro-peritectic phase LiOH and 25%wt of the LiBr solid phase.

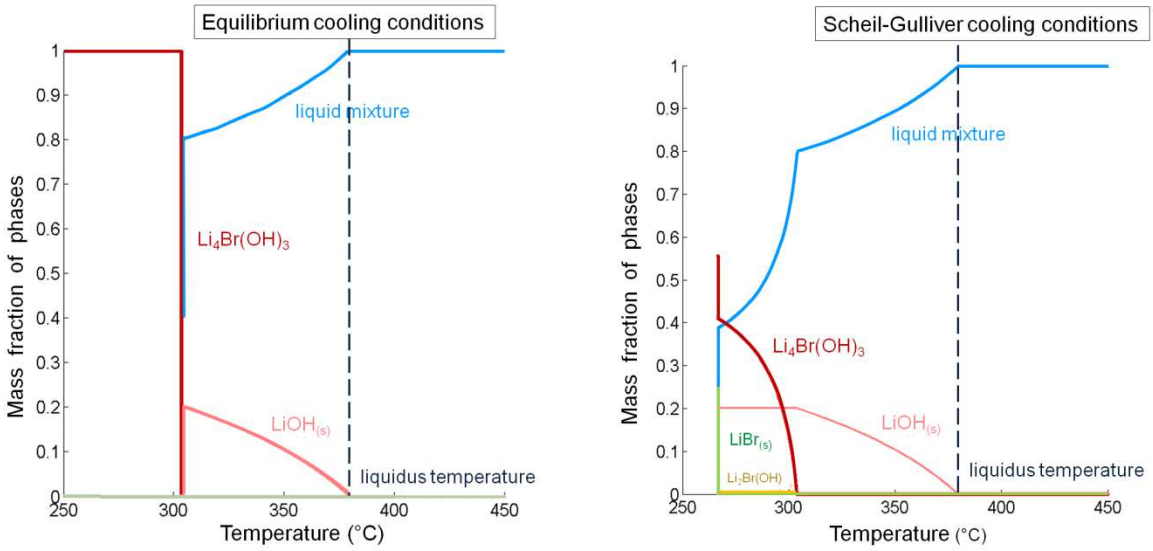

(a) (b)

Figure 6. Theoretical evolution of the mass phase fractions with temperature for $Li_4Br(OH)_3$ under: (a) thermodynamic equilibrium and (b) Scheil–Gulliver cooling conditions.

Figure 7 shows the raw DSC stepscan mode data and the baseline response generated by $Li_4Br(OH)_3$ after its synthesis inside a free-cooled furnace. These results correspond to the third improved protocol (Subsection 2.2.2). In the first two experiments, $Li_4Br(OH)_3$ was synthesized directly in the DSC furnace and the heat flux did not have sufficient time to return to the 0 value, thereby preventing the determination of the good baseline required for the enthalpy calculation (which was obtained in the third experiment, as shown in the inset in Fig. 7). The baseline allowed us to consider the thermal lag and to determine the specific heat capacity of the sample. The thermal lag was due to the temperature gradient inside the sample, but it could also have been related to the difference between the temperature program applied and the sample temperature induced by the temperature gradients along the heat flow path.

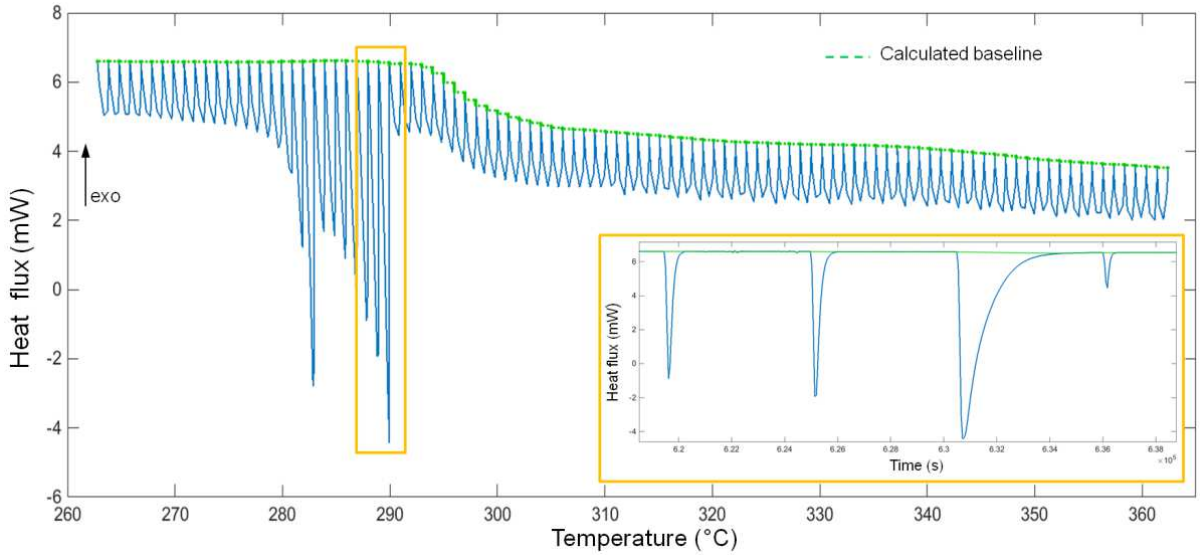

Figure 7. DSC stepscan run obtained at temperatures from 260℃ to 360°C for $Li_4Br(OH)_3$ at 1°C temperature increases, with ramping at 0.5℃/min, and followed by 60-min isothermal holds. Argon was used as the purge gas with cooling. The inset shows the corresponding heat flux over time and its related baseline as the green line.

The enthalpy-temperature functions were calculated for all of the experiments and the results were compared with those obtained for the two extreme cases under equilibrium and Scheil–Gulliver cooling conditions using FactSage 7.0® software. The results are presented in Fig. 8, which show that: (i) the experimentally obtained peritectic transition temperature value (290°C) was in very good agreement with those determined experimentally in previous studies [13, 14, 18]; (ii) the eutectic transition value was not observed at the predicted value of 267°C, but a transition at 283°C (Figs 7 and 8) agreed better with the values detected previously [16]; and (iii) a peritectoid transition was not observed at the reported values (245–250°C) but a transition (not shown) was observed at a lower temperature of 231°C.

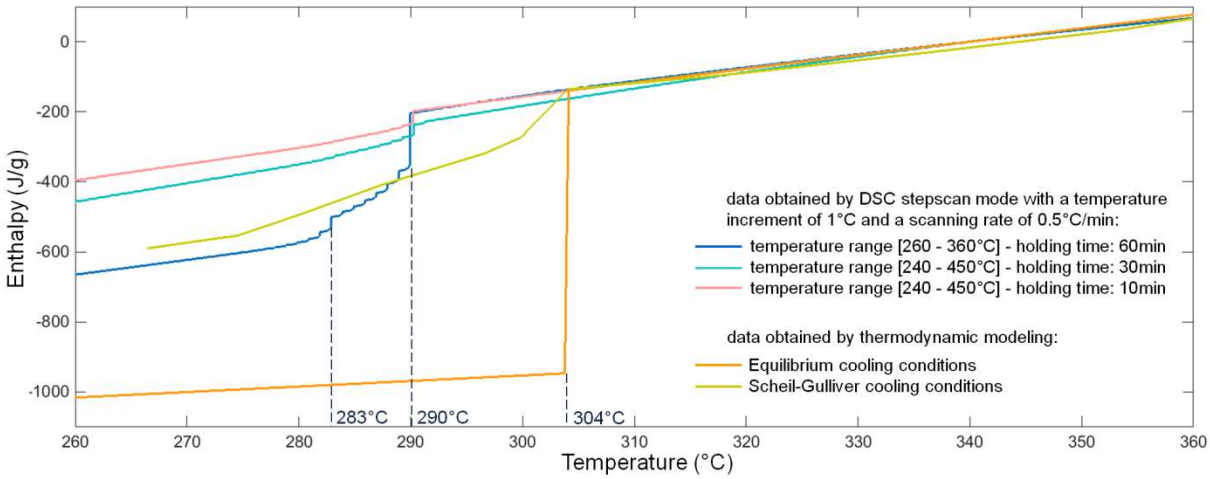

Figure 8. Experimental changes in the enthalpy for $Li_4Br(OH)_3$ (with respect to the enthalpy for the reference) with temperature obtained at ambient pressure using three different protocols in the DSC stepscan mode, and compared with those calculated under equilibrium and Scheil–Gulliver cooling conditions.

Considering the caution given by Kroupa [11] regarding the temperature uncertainty of ± 20°C (see Subsection 3.1), the data from the best experiment were shifted by 14°C to adjust the calculated peritectic temperature (304°C). Figure 9 compares the results with those calculated theoretically for the two extreme cases. Initially, the experimental data matched perfectly with those obtained under

equilibrium cooling conditions, but they then deviated out-of-equilibrium to follow the same trend in the data calculated for Scheil–Gulliver conditions. The solidification path that satisfied the equilibrium conditions had an enthalpy of 800 J/g at a constant temperature of 304°C, whereas the path that satisfied the Scheil–Gulliver conditions had an enthalpy of 450 J/g over a temperature of 37°C. The compound obtained had an available gravimetric energy density related to the global first order transition jump of 380 J/g over a temperature of around 10°C. This value was 300 J/g after subtracting the part related to the potential eutectic transition and it decreased to 170 J/g when only the first part of the signal was considered.

These observations strongly suggest that it would be useful to fully characterize the thermophysical properties of this compound to assess its possible utilization as a thermal energy storage material for applications around 300°C. We observed a mass loss of 33% during the experiment despite trying to ensure that the crucible would not leak, and thus the assessed values were greatly underestimated. XRD analysis indicated the presence of $Li_4Br(OH)_3$, LiOH, and LiBr-H_2O among the end products, which demonstrates that the LiOH pro-peritectic phase was not completely consumed to form $Li_4Br(OH)_3$, as predicted (Fig. 6b).

Finally, the thermodynamic model was reliable given that the experimental results were between the two theoretical extreme cases and considering the temperature uncertainty of ± 20°C. However, further experimental investigations should be performed of different compositions to refine and update the proposed model, particularly in terms of thermal energy storage.

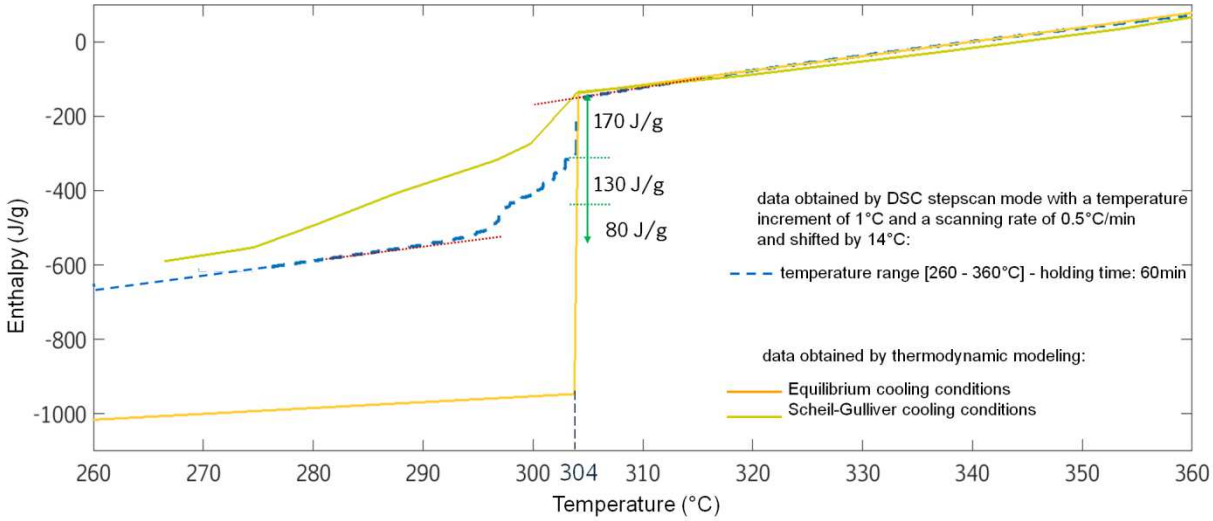

Figure 9. Experimental changes in the enthalpy of $Li_4Br(OH)_3$ (with respect to the enthalpy of the reference) with temperature at ambient pressure obtained in the DSC stepscan mode with a holding time of 60 min, where the results are shifted by 14°C and compared with those calculated under equilibrium and Scheil–Gulliver cooling conditions.

4. Conclusion

In this theoretical study of the LiBr/LiOH system phase diagram, we identified one of the most promising peritectic compounds for use as a heat storage material. The successful synthesis of $Li_4Br(OH)_3$ and its thermal characterization showed that this new material may provide comparable or even higher energy compared with the best solid–gas reactions under development. Moreover, in contrast to thermochemical heat storage materials, $Li_4Br(OH)_3$ does not require advanced complex technology for its production.

The expected volumetric and gravimetric energy densities are much higher than those for the currently employed phase change materials, so the investment cost should be lower than that in latent heat storage technologies and probably closer to that for the cheapest sensible heat storage options. Therefore, $Li_4Br(OH)_3$ may allow ultra-compact thermal energy storage at an attractive investment

cost as well as operating at almost constant temperature and under ambient pressure. Thus, $Li_4Br(OH)_3$ is an attractive material that requires further study and characterization, particularly its chemical stability and compatibility with materials used for containment tanks and heat exchangers.

Acknowledgement

The authors acknowledge financial support from the ANR for subsidizing Pc2TES: ANR-16-CE06-0012-01 project.

References

[1] Felderhoff M. et al. Thermochemical heat storage for high temperature applications: A review. Green, 2013, 3: 133–123.

[2] Wei G., Wang G., Xu C., Ju X., Xing L., Du X., Yang Y. Selection principles and thermophysical properties of high temperature phase change materials for thermal energy storage: A review. Renewable and Sustainable Energy Reviews, 2018, 81: 1771–1786.

[3] R. Tamme et al. Latent heat storage for solar steam systems. Journal of Solar Energy Engineering, 2008, 130: 1–5. doi:10.1115/1.2804624

[4] Crespo A., Barreneche C., Ibarra M., Platzer W. Latent thermal energy storage for solar process heat applications at medium-high temperatures - A review. Solar Energy, 2018, https://doi.org/10.1016/j.Solener.2018.06.101

[5] Kenisarin M.M. High-Temperature phase change materials for thermal energy storage. Renewable and Sustainable Energy Reviews, 2010, 27: 724–737.

[6] Pielichowska K., Pielichowski K. Phase change materials for thermal energy storage. Progress in Materials Science, 2014, 65: 67–123.

[7] Alva G., Lin Y., Fang G. An overview of thermal energy storage systems. Energy, 2018, 144: 341–378.

[8] Yang Y., Wang L., Snead L., Zinkle S.J. Development of novel Cu-Cr-Nb-Zr alloys with the aid of computational thermodynamics. Materials and Design, 2018, 156: 370–380.

[9] Schmid-Fetzer R. Phase diagrams: the beginning of wisdom. Journal of Phase Equilibria and Diffusion, 2014, 35: 735–760.

[10] Saunders N., Miodownik A.P. CALPHAD Calculation of Phase Diagrams - A Comprehensive Guide. Pergamon Press, 1998.

[11] Kroupa A. Modelling of phase diagrams and thermodynamic properties using *Calphad* method - Development of thermodynamic databases. Computational Materials Science, 2013, 66: 3–13.

[12] Sangster J. Thermodynamics and phase diagrams of 32 binary common-systems of the group Li, Na, K, Rb, Cs//F, Cl, Br, I, OH, NO_3: basic and applied research section I. Journal of Phase Equilibria, 2000, 21: 241–268.

[13] Liu M., Gomez J.C., Turchi C.S., Tay N.H.S., Saman W., Bruno F. Determination of thermo-physical properties and stability testing of high-temperature phase change materials for CSPs applications. Solar Energy Materials & Solar Cells, 2015, 139: 81–87.

[14] Hartwig p., Weppner W. Ionic conductivities of lithium-halide-based quaternary compounds. Solid State Ionics, 1981, 3/4: 249–254.

[15] Scarpa G.: Atti Real. Accad. Lincei, Sez. II, 1915, 24: 476; 738; 955 (in Italian).

[16] Sangster J., Pelton A.D. Phase diagrams and thermodynamic properties of the 70 binary alkali-halide systems having common ions. Journal of Physical and Chemical Reference Data, 1987, 16: 509–561.

[17] Reshetnikov N.A., Unzhakov G.M. Izv. Fiz.-Khim Nauch.-Issled. Inst. Irkutsk. Gosud. Univ. 1953, 2: 23 (in Russian).

[18] Friese K., Hönnerscheid A., Jansen M. Crystal structure determination of systematically intergrown compounds: $Li_5Br_3(OH)_2$ and $Li_2Br(OH)$. Z. Kristallogr., 2003, 536–541.

[19] Levin E.M., Robbins C.R. Phase Diagram for Ceramists VII: Salts. American Ceramic Society, 1989.
[20] Gulliver G.M. The quantitative effect of rapid cooling upon the constitution of binary alloys. Journal of the Institute of Metals, 1913, 9:120–157.
[21] Schaffnit P., Stallybrass C., Konrad J., Frank S., Neti S. A Scheil-Gulliver model dedicated to the solidification of steel. CALPHAD: Computer Coupling of Phase Diagrams and Thermochemistry, 2015, 48: 184–188.
[22] Wang L., Dong J., Tian Y., Zhang L. Microsegregation and Rayleigh number variation during the solidification of superalloy Inconel 718. Journal of University of Science and Technology Beijing, 2008, 15: 594–599.
[23] Hönnerscheid A., Nuss J., Mühle C., Jansen M. Die Kristallstrukturen der Hydroxyhalogenide $Li_4(OH)_3Br$ und $Li_4(OH)_3I$. Z. Anorg. Allg. Chem., 2003, 629: 317–320.

FIGURES WITH CAPTIONS

FIGURE 1

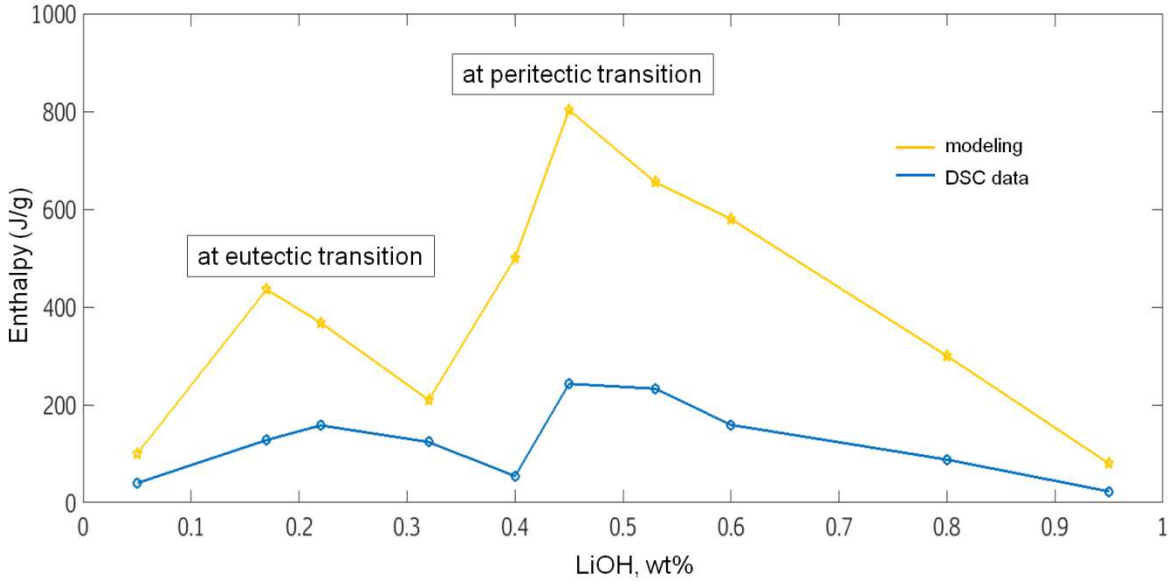

Figure 1. Gravimetric energy density dependence with LiOH mass fraction considering only the peritectic and eutectic transitions (calculated values are the difference between enthalpy and enthalpy of reference in yellow and DSC data (in red)).

FIGURE 2

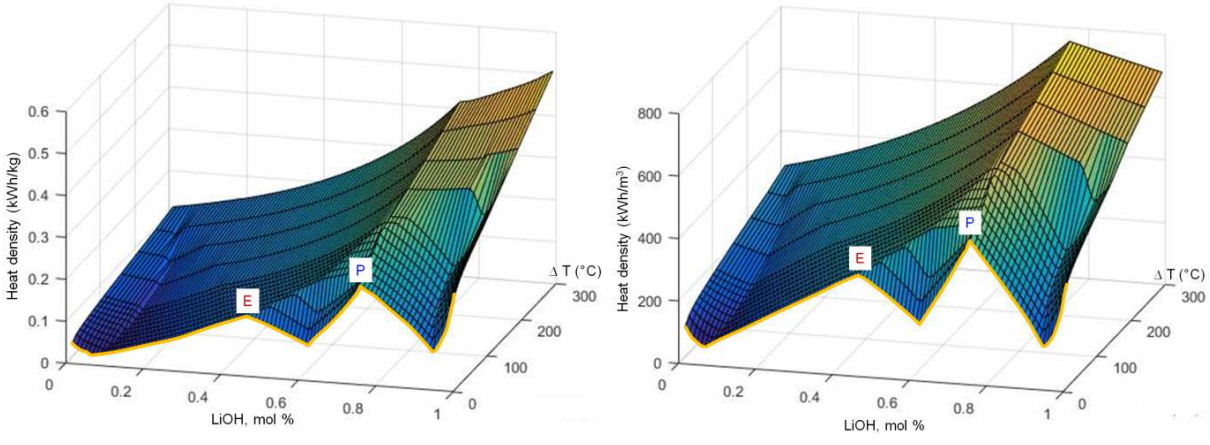

a/ b/

Figure 2. Theoretical heat densities dependence with LiOH molar fraction, at ambient pressure and for a temperature variation of ΔT = 300°C: a/ gravimetric heat density; b/ volumetric heat density.

FIGURE 3

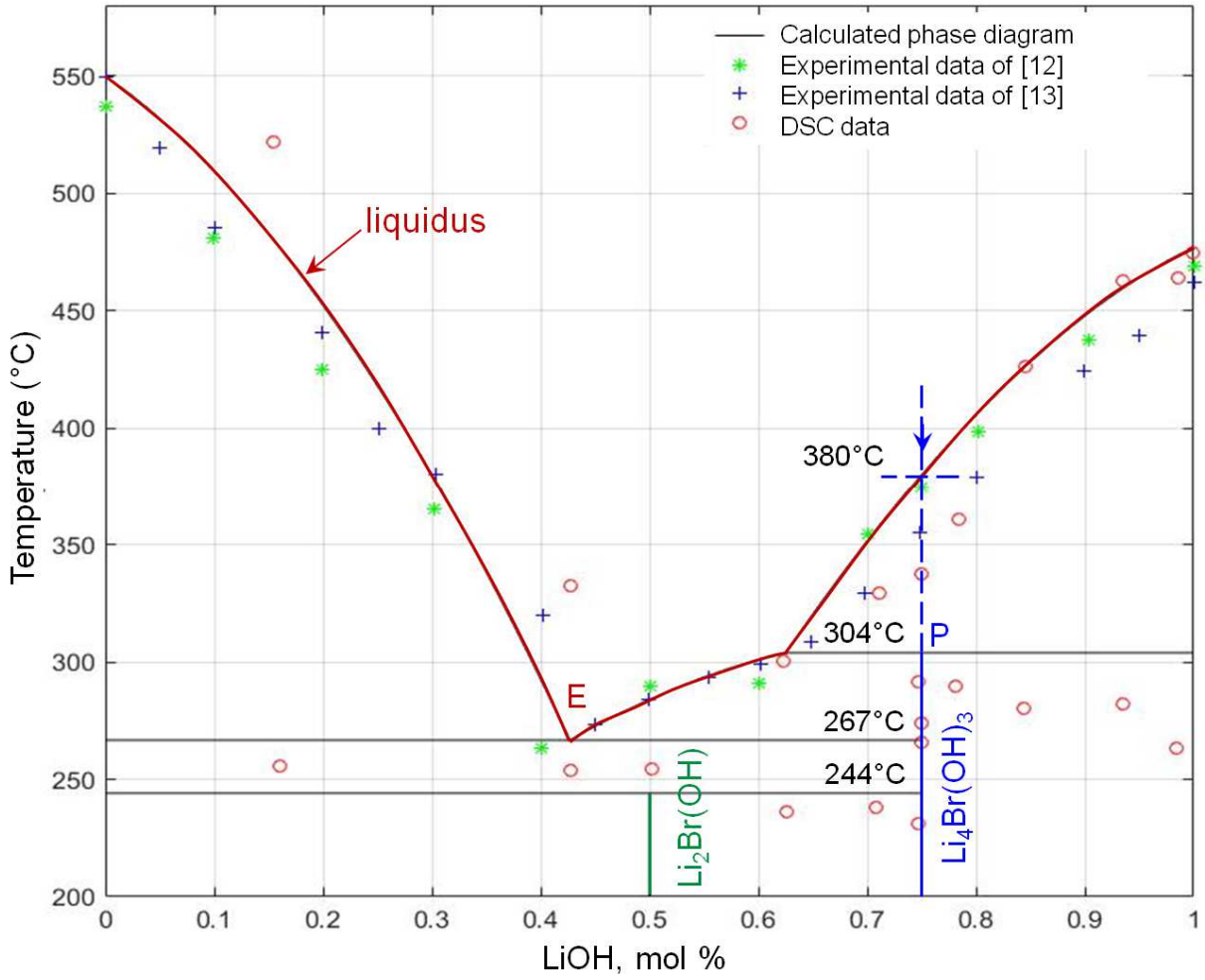

Figure 3. DSC data (red circles) with literature values (blue and green points) overlaid with the calculated LiBr/LiOH binary system phase diagram, obtained for equilibrium conditions at ambient pressure (liquidus line in red). The nominal alloy composition specifically sought after is highlighted here by the blue dashed line.

FIGURE 4

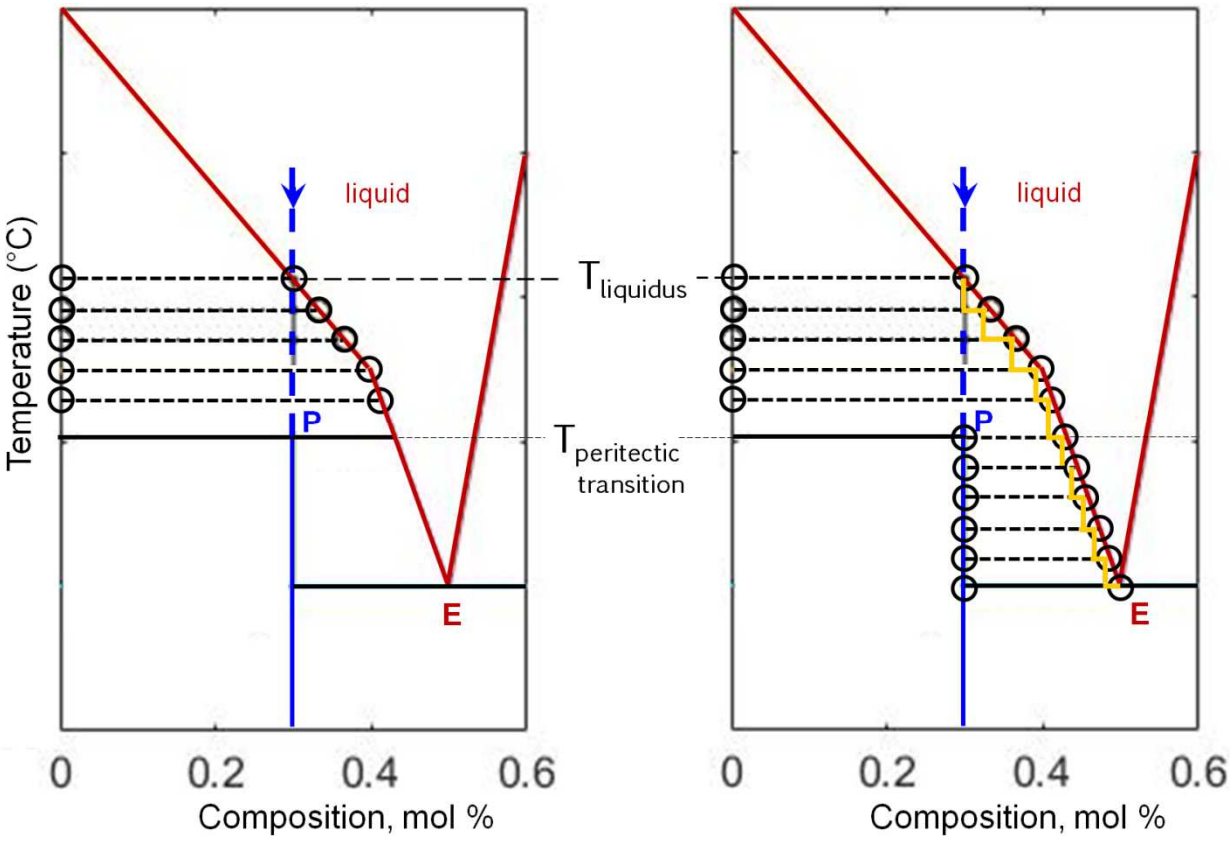

a/ b/

Figure 4. Paths in series of a/ quasi-equilibrium steps (level rule), going from the liquidus line to the peritectic transition, and b/ of out-of-equilibrium steps (Scheil-Gulliver), going from the liquidus line to the eutectic transition.

FIGURE 5

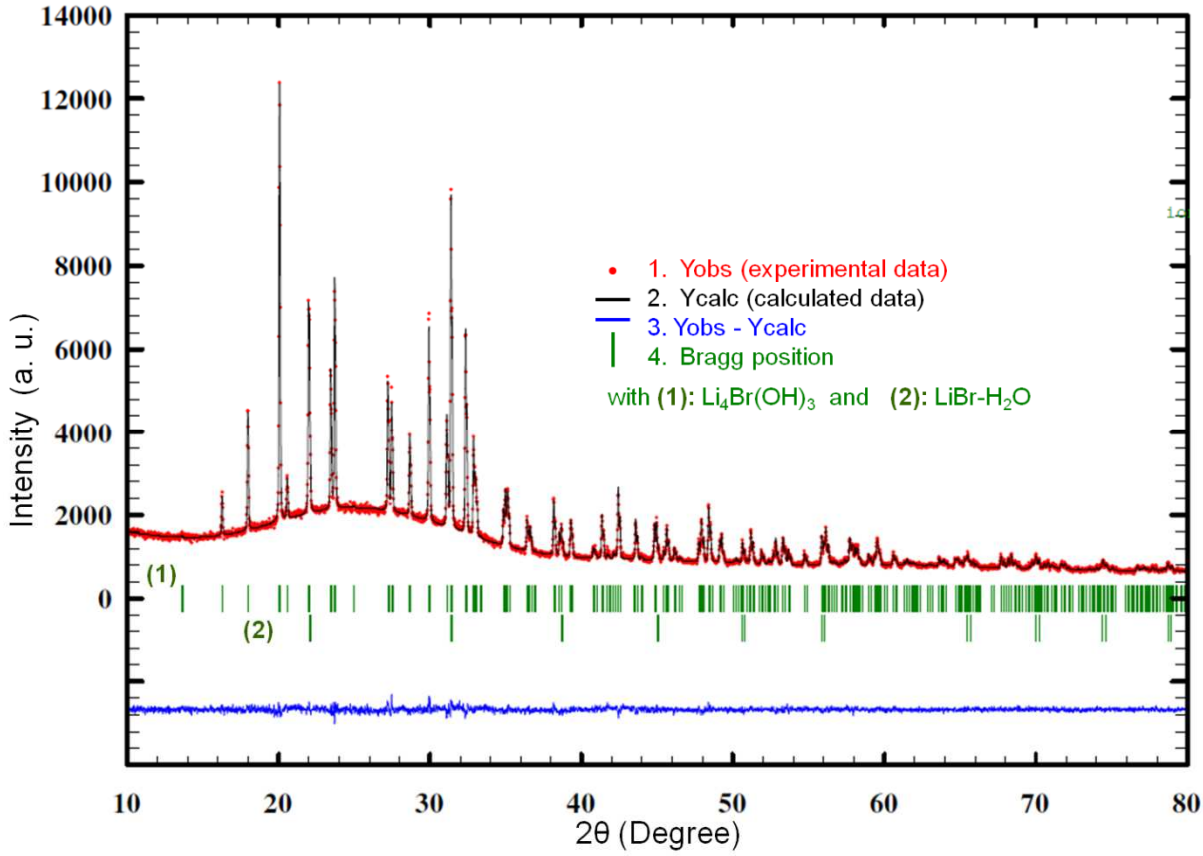

Figure 5. Rietveld plot of $Li_4Br(OH)_3$ with above: measured intensity (red points), calculated intensity (black line), and at the bottom: Bragg positions and plot of differences.

FIGURE 6

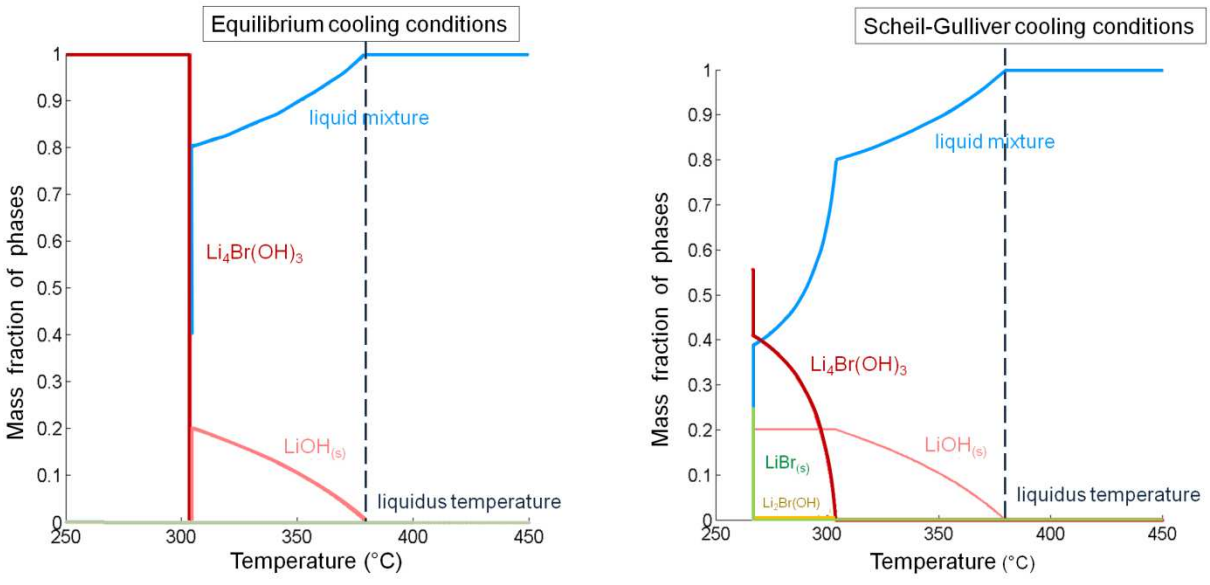

a/ b/

Figure 6. Theoretical evolutions of the mass phase fractions with temperature for $Li_4Br(OH)_3$ under a/ thermodynamic equilibrium and b/ Scheil-Gulliver cooling conditions.

FIGURE 7

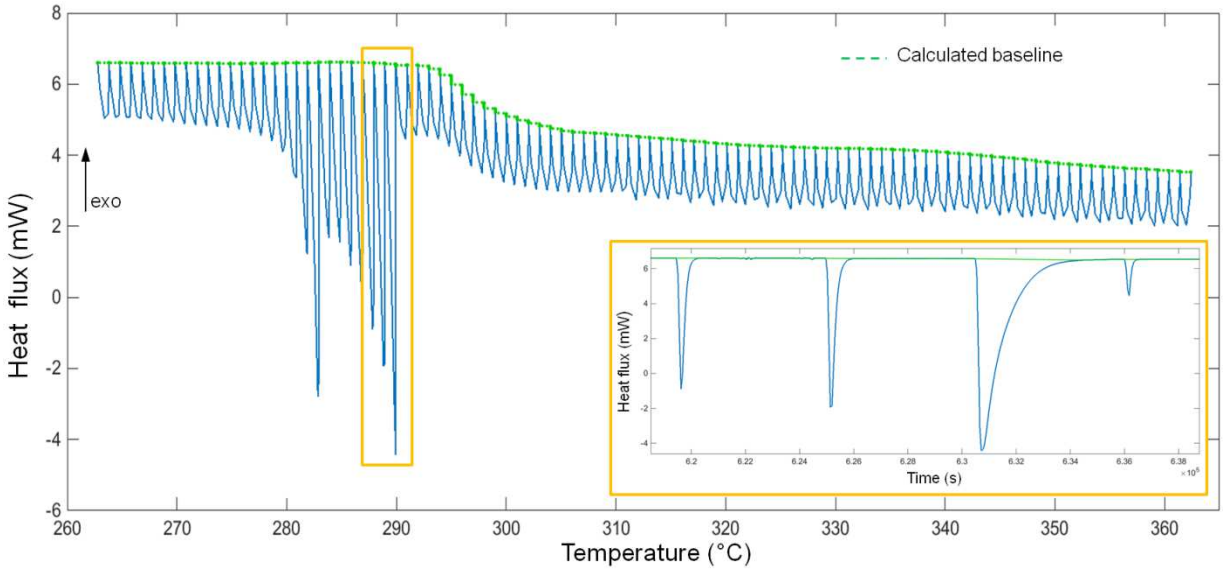

Figure 7. DSC stepscan run obtained for temperature varying from 260 to 360°C on $Li_4Br(OH)_3$ applying 1°C temperature jumps increases, ramped at 0.5 °C/min and followed by 60 min isothermal holds. Argon was used for the purge gas with cooling. The inlay showed the corresponding heat flux with time and its related baseline in green line.

FIGURE 8

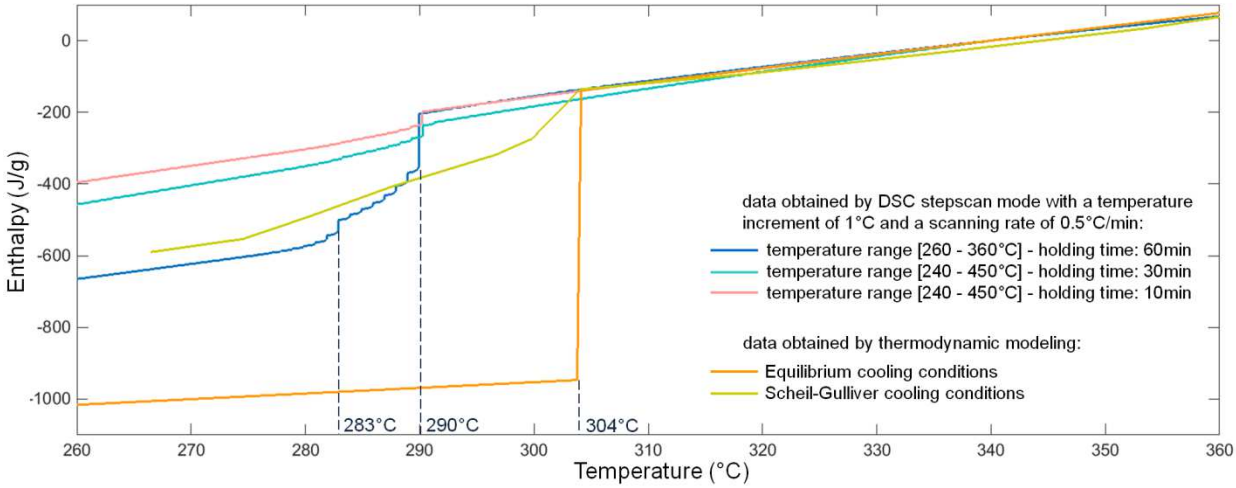

Figure 8. Experimental enthalpy evolutions of $Li_4Br(OH)_3$ (with respect of the enthalpy of reference) with temperature, at ambient pressure, obtained with three different protocols by DSC stepscan mode and compared with the calculated ones, at equilibrium and Scheil-Gulliver cooling conditions.

FIGURE 9

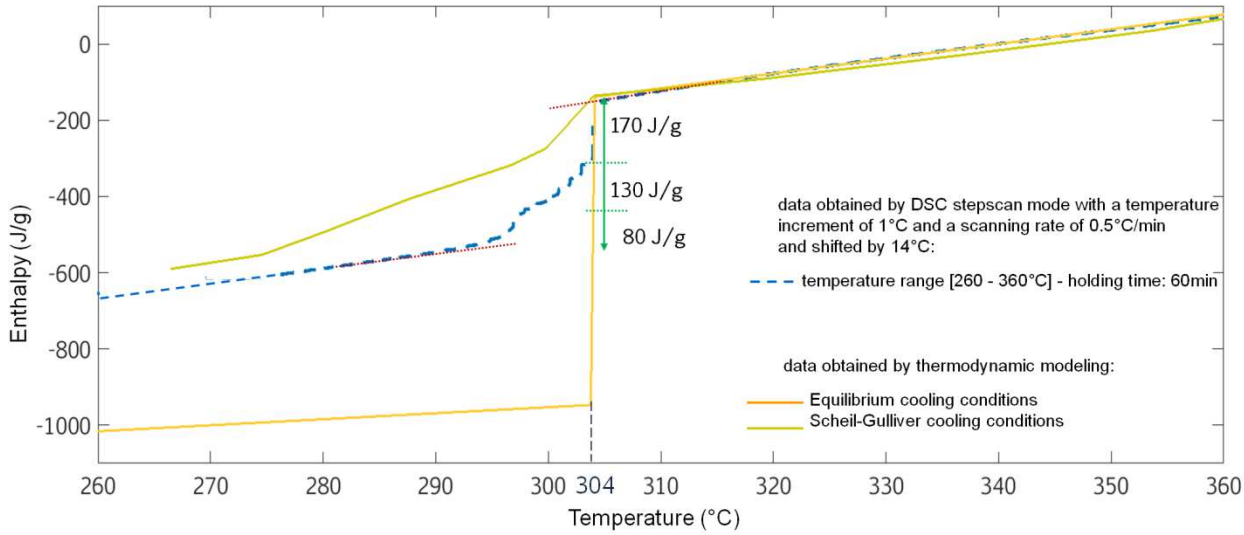

Figure 9. Experimental enthalpy evolution of $Li_4Br(OH)_3$ (with respect of the enthalpy of reference) with temperature, at ambient pressure, obtained by DSC stepscan mode for a holding time of 60 min, shifted by 14°C and compared with the calculated ones, at equilibrium and Scheil-Gulliver cooling conditions.

TABLES WITH CAPTIONS

Chemicals	LiBr		LiOH	
Supplier	Acros Organics	FactSage 7.0®	Acros Organics	FactSage 7.0®
Purity (%)	99+	-	98	-
Molar mass (g/mol)	86.84	86.845	23.95	23.948
Fusion temperature (°C)	552	549.85	462	477

Table 1 Comparison of the molar mass and of the fusion temperature values provided by the chemicals supplier with the values from FactSage software database for each used chemical.

Composition n°	LiBr/LiOH (mol%)	LiBr/LiOH (wt%)	ΔH (J/g)	TTr (°C)	TL (°C)
1/ LiBr	100/0	100	203	-	549.85
2/ Eutectic	58/42	83/17	- 436	244.12 266.69	266.69
3/ Li2BrOH	50/50	78/22	2.00 366	244.12 266.69	284.02
4/	37/63	68/32	- 212	244.12 266.69	303.90
5/	29/61	60/40	35.0 244 495	244.12 266.69 303.90	355.78
6/ Li4Br(OH)3	25/75	55/45	803	303.90	379.89
7/	16/84	50/50	733	303.90	397.60
8/	29/61	40/60	587	303.90	426.00
9/	6/94	20/80	293	303.90	459.72
10/	1.4/98.6	5/95	70.0	303.90	473.66
11/ LiOH	0/100	100	875	-	477.00

Table 2 Thermophysical properties of compositions used to experimentally screen the whole composition range of the LiBr/LiOH binary system on basis of the calculated phase diagram. T_{Tr} is the transition temperatures encountered by each defined composition. T_L is the corresponding liquidus temperature (Cf. Figure 3).

Compounds	LiBr/LiOH (mol%)	LiBr/LiOH (wt%)	ρ_L (g/cm^3)	ρ_S (g/cm^3)	ΔV/V (%)	Tm (°C)	ΔH (J/g^{-1})	E (kWh/m^{-3})
LiBr	100/0	100	2.871	3.464	-	549.85	203	195
Eutectic	58/42	83/17	-	2.373	15	266.69	436	287
Li2BrOH	50/50	78/22	-	2.671	-	244.12	2.00	1.51
Li4Br(OH)3	25/75	55/45	-	1.945	9	303.90	803	434
LiOH	0/100	100	1.582	3.464	-	477.00	875	356

Table 3 Key thermophysical properties of specific compounds observed in the calculated phase diagram.